

Star-in-a-box simulations of fully convective stars

P. J. Käpylä^{1,2}

¹ Georg-August-Universität Göttingen, Institut für Astrophysik, Friedrich-Hund-Platz 1, D-37077 Göttingen, Germany e-mail: pkaepyl@uni-goettingen.de

² Nordita, KTH Royal Institute of Technology and Stockholm University, SE-10691 Stockholm, Sweden

January 28, 2022

ABSTRACT

Context. Main-sequence late-type stars with masses less than $0.35M_{\odot}$ are fully convective.

Aims. To study convection, differential rotation, and dynamos as functions of rotation in fully convective stars.

Methods. Three-dimensional hydrodynamic and magnetohydrodynamic numerical simulations in a star-in-a-box model, where a spherical star is immersed inside of a Cartesian cube, are used. The model corresponds to a $0.2M_{\odot}$ main-sequence M5 dwarf. A range of rotation periods (P_{rot}) between 4.3 and 430 days is explored.

Results. The slowly rotating model with $P_{\text{rot}} = 430$ days produces anti-solar differential rotation with a slow equator and fast poles, along with predominantly axisymmetric quasi-steady large-scale magnetic fields. For intermediate rotation ($P_{\text{rot}} = 144$ and 43 days) the differential rotation is solar-like (fast equator, slow poles) and the large-scale magnetic fields are mostly axisymmetric and either quasi-stationary or cyclic. The latter occurs in a similar parameter regime as in other numerical studies in spherical shells, and the cycle period is similar to observed cycles in fully convective stars with rotation periods of roughly 100 days. In the rapid rotation regime the differential rotation is weak and the large-scale magnetic fields are increasingly non-axisymmetric with a dominating $m = 1$ mode. This large-scale non-axisymmetric field also exhibits azimuthal dynamo waves.

Conclusions. The results of the star-in-a-box models agree with simulations of partially convective late-type stars in spherical shells in that the transitions in differential rotation and dynamo regimes occur at similar rotational regimes in terms of the Coriolis (inverse Rossby) number. This similarity between partially and fully convective stars suggests that the processes generating differential rotation and large-scale magnetism are insensitive to the geometry of the star.

Key words. Stars: magnetic field – Dynamo – Magnetohydrodynamics (MHD) – Convection – Turbulence

1. Introduction

The existence of fully convective low-mass stars has been predicted by theoretical stellar models at least since the 1950s (e.g. Limber 1958). Current stellar structure and evolution models indicate that stars with masses less than about $0.35M_{\odot}$ are fully convective (e.g. Chabrier & Baraffe 1997, 2000). However, until recently no direct observational evidence could be attached to this transition. A recent analysis of GAIA observations indicates a gap in the main sequence at spectral type M3 which is perhaps the most direct observational evidence of transition to full convection to date (Jao et al. 2018). The gap in the Hertzsprung–Russell diagram near the transition to full convection is presumed to be associated with an instability related to ^3He burning in the core of the star, such the core undergoes periods of radiative and convective phases before settling to a final either convectively stable or unstable state depending on the mass of the star (e.g. van Saders & Pinsonneault 2012; Baraffe & Chabrier 2018; Feiden et al. 2020). Furthermore, in the final stable configuration, stars just on the partially convective side of the transition have a substantial (roughly 40 per cent of stellar radius) radiative core, implying a discontinuity in stellar structure around $M = 0.35M_{\odot}$.

The transition to full convection is important from the point of view of stellar dynamo theory because of an ongoing debate regarding the origin of the solar large-scale magnetic field (e.g. Charbonneau 2020, and references therein). This debate revolves around the importance of the tachocline, a layer of strong shear just below the convection zone (CZ), and that of

the convection zone itself. In simplified terms, the distributed dynamo scenario the magnetic fields are generated throughout the CZ and the tachocline is unimportant (e.g. Krause & Rädler 1980; Brandenburg 2005; Käpylä et al. 2006; Pipin & Kosovichev 2011), while in the flux-transport models (e.g. Dikpati & Charbonneau 1999; Hazra et al. 2014) the roles of the two are opposite although in reality stellar dynamos are likely to have ingredients from both scenarios.

The fact that there are no tachoclines in fully convective stars makes these objects highly interesting in view of dynamo theory. If M star magnetism would show a discontinuity at the transition to full convection, one could argue that also the type of dynamo changes across the transition. However, no conclusive observational evidence for such discontinuity has been detected so far (Donati et al. 2008; Morin et al. 2008, 2010; Kochukhov 2020), such that most activity indicators appear to be continuous across the transition to full convection (see, however, West et al. 2015; Mullan & Houdebine 2020). For example, the X-ray luminosity of fully convective M stars falls in line with partially convective stars (Wright & Drake 2016; Wright et al. 2018).

Observations of M stars shows a rich variety of possible magnetic states (see Kochukhov 2020, and references therein). Zeeman-Doppler Imaging (ZDI) results of early-type (partially convective) M dwarfs tend to have relatively weak multipolar fields while stars around the transition to full convection often have strong dipole-dominated configurations (Donati et al. 2008). Intriguingly, rapidly rotating late-type M dwarfs can have either configuration, suggesting a possibility of bistable dynamo

states (e.g. Gastine et al. 2013). The ZDI results of fully convective stars have not yet revealed any cyclicity, for example in terms of polarity reversals of the large-scale field. The lack of sufficiently long data series is a likely contributor to this. However, longer term observations of other activity indicators, such as chromospheric emission, of a nearby slowly rotating ($P_{\text{rot}} \approx 90$ days) fully convective star Proxima Centauri indicate an activity cycle of around seven years (Su  rez Mascare  o et al. 2016; Wargelin et al. 2017; Klein et al. 2020; Damasso et al. 2020). Another recent study found evidence of an activity cycle of roughly 5 years for the fully convective star Ross 128 with rotation period of more than 100 days (Iba  ez Bustos et al. 2019, and references therein). Interestingly, an activity cycle of similar length has also been reported recently from a rapidly rotating fully convective star Gl 729 with $P_{\text{rot}} \approx 3$ days (e.g. Iba  ez Bustos et al. 2020).

Another aspect that makes low mass stars particularly interesting is that detecting Earth-sized planets on orbits suitable for life around M stars is much easier than for, for example, solar mass stars. This is because M stars are less massive than the Sun, and due to their low luminosity the habitable planets must have close orbits, leading to a much larger radial velocity signal (e.g. Kasting et al. 2014). However, as noted above, M stars are very often magnetically active which leads to effects such as starspots and Zeeman broadening which can hinder radial velocity measurements. The magnetic activity of the host star is also of significance for the exoplanets such that they can be subject to violent flares and coronal mass ejections. Therefore, understanding convection and magnetic activity of M stars is of great importance in the search for possible life-supporting exoplanets.

Numerical simulations of fully convective stars are challenging due to the fact that the convection zone (CZ) spans the entire radius of the star, implying strong density contrast and greatly varying spatial and temporal scales. Furthermore, the Mach numbers in the cores of fully convective stars are very low leading to a short acoustic timestep. A further complication arises due to the singularity of commonly used spherical polar coordinates at the centre of the star. Most three-dimensional simulations of fully convective stars to date (e.g. Browning 2008, 2011; Gastine et al. 2013; Yadav et al. 2015a, 2016; Brown et al. 2020) have been made using anelastic equations which bypass the acoustic time step constraint. Furthermore, most of these simulations operate in spherical shells and the innermost core of the star is not modeled due to the coordinate singularity (see, however, Brown et al. 2020). Although it can be argued that the omission of a small core spanning at most a few per cent of stellar radius is likely to be insignificant for the global dynamics, additional boundary conditions need to be imposed around the central void. An exception is the study of Dobler et al. (2006) who used a star-in-a-box approach (see also Freytag et al. 2002; Dorc 2004; Woodward et al. 2019) where a spherical star is embedded into a Cartesian cube. This approach allows the full star, including the centre, to be modeled. However, this comes at a cost of including the corners of the box that are unimportant for the interior dynamics of the star. This also implies that the spatial resolution of the star-in-a-box simulations is necessarily lower than in corresponding spherical shells models.

In the current study the star-in-a-box model of Dobler et al. (2006) is refined with developments from convection simulations in other contexts. This includes using heat conductivity based on Kramers opacity law (e.g. Brandenburg et al. 2000; K p l  et al. 2017b) and a subgrid-scale entropy diffusion that enables more realistic luminosities. Furthermore, one of the principal aims of the current study is to compare the results from the

star-in-a-box models of fully convective stars with corresponding results obtained in spherical shells. Another point of interest is to compare the transitions of differential rotation and dynamo solutions as functions of rotation in fully convective stars. Numerical studies of partially convective stars indicate a transition from anti-solar (slow equator, fast poles) to solar-like (fast equator, slow poles) differential rotation (e.g. Gastine et al. 2014; K p l  et al. 2014) around the rotation rate where the advection and Coriolis forces are of the same order of magnitude, that is Coriolis (inverse Rossby) number unity. Furthermore, corresponding dynamo solutions progress from predominantly axisymmetric and quasi-steady solutions for slow rotation (e.g. K p l  et al. 2017a; Strugarek et al. 2018), through oscillatory axisymmetric fields at intermediate rotation (e.g. Gilman 1983; K p l  et al. 2012; Nelson et al. 2013), to non-axisymmetric azimuthal dynamo waves for rapid rotation (e.g. Cole et al. 2014; Viviani et al. 2018). A set of simulations with rotation periods in the range from 4.3 to 430 days are presented to study if, and where, such transitions in differential rotation and dynamos occur also in models of fully convective stars.

2. The model

The models is based on the star-in-a-box model presented in Dobler et al. (2006). A star of radius R is embedded into a Cartesian cube with a side half-length of $H = 1.1R$. Motions and thermodynamic fluctuations are damped for $r > R$ where $r = \sqrt{x^2 + y^2 + z^2}$ is the spherical radius. The following set of equations of magnetohydrodynamics (MHD) are solved:

$$\frac{\partial \mathbf{A}}{\partial t} = \mathbf{U} \times \mathbf{B} - \eta \mu_0 \mathbf{J}, \quad (1)$$

$$\frac{D \ln \rho}{Dt} = -\nabla \cdot \mathbf{U}, \quad (2)$$

$$\frac{D\mathbf{u}}{Dt} = -\nabla \Phi - \frac{1}{\rho} (\nabla p - \nabla \cdot 2\nu \rho \mathbf{S} + \mathbf{J} \times \mathbf{B}) - 2\boldsymbol{\Omega} \times \mathbf{U} + \mathbf{f}_d, \quad (3)$$

$$T \frac{Ds}{Dt} = -\frac{1}{\rho} [\nabla \cdot (\mathbf{F}_{\text{rad}} + \mathbf{F}_{\text{SGS}}) + \mathcal{H} - \mathcal{C}] + 2\nu \mathbf{S}^2 + \mu_0 \eta \mathbf{J}^2, \quad (4)$$

where $D/Dt = \partial/\partial t + \mathbf{U} \cdot \nabla$ is the advective derivative, \mathbf{A} is the magnetic vector potential, \mathbf{U} is the velocity, $\mathbf{B} = \nabla \times \mathbf{A}$ is the magnetic field, $\mathbf{J} = \nabla \times \mathbf{B}/\mu_0$ is the current density, μ_0 is the permeability of vacuum, η is the magnetic diffusivity, ρ is the fluid density, Φ is the gravitational potential, p is the pressure, ν is the kinematic viscosity, \mathbf{S} is the traceless rate-of-strain tensor with

$$S_{ij} = \frac{1}{2}(U_{i,j} + U_{j,i}) - \frac{1}{3}\delta_{ij} \nabla \cdot \mathbf{U}, \quad (5)$$

where the commas denote differentiation and δ_{ij} is the Kronecker delta. $\boldsymbol{\Omega} = (0, 0, \Omega_0)$ is the rotation rate of the star, \mathbf{f}_d is a damping function, T is the temperature, s is the specific entropy, \mathbf{F}_{rad} is the radiative flux, \mathbf{F}_{SGS} is the subgrid-scale entropy flux, and \mathcal{H} and \mathcal{C} describe heating and cooling, respectively.

The gas obeys an ideal gas equation of state with $p = \mathcal{R}\rho T$, where $\mathcal{R} = c_p - c_v$ is the universal gas constant, and c_p and c_v are the heat capacities at constant pressure and volume, respectively. The gravitational potential Φ is fixed in space and time, and set up such that it corresponds to an isentropic hydrostatic

state of an M5 star (see Appendix A of Dobler et al. 2006) with

$$\Phi(r) = -\frac{GM}{R} \frac{a_0 + a_2 r'^2 + a_3 r'^3}{1 + b_2 r'^2 + b_3 r'^3 + a_3 r'^4}, \quad (6)$$

where G is the gravitational constant, M is the mass of the star, $r' = r/R$ and $a_0 = 2.34$, $a_2 = 0.44$, $a_3 = 2.60$, $b_2 = 1.60$, and $b_3 = 0.21$.

The term f_d describes damping of flows exterior to the star according to

$$f_d = -\frac{U}{\tau_{\text{damp}}} f_e(r), \quad (7)$$

where τ_{damp} is a damping timescale, and where $f_e(r)$ is given by

$$f_e(r) = \frac{1}{2} \left(1 + \tanh \frac{r - r_{\text{damp}}}{w_{\text{damp}}} \right), \quad (8)$$

where $r_{\text{damp}} = 1.03R$ and $w_{\text{damp}} = 0.03R$. The damping timescale, $\tau_{\text{damp}} \approx 1$ day, is short in comparison to all other relevant timescales in the system.

Radiation is taken into account though the diffusion approximation. The radiative flux is given by

$$F_{\text{rad}} = -K \nabla T, \quad (9)$$

where

$$K(\rho, T) = K_0(\rho/\rho_0)^{a-1} (T/T_0)^{b+3}. \quad (10)$$

Here $a = -1$ and $b = 7/2$ are chosen corresponding to the Kramers opacity law that describes the average opacity for bound-free and free-free transitions (e.g. Carroll & Ostlie 2013). The Kramers opacity law was first used in convection simulations by Brandenburg et al. (2000), but has been adopted more widely only recently (K  p  l   et al. 2017b; K  p  l   2019b; K  p  l   et al. 2020; Viviani & K  p  l   2020).

Using the Kramers heat conductivity entails that the diffusion of entropy fluctuations depends strongly on density and temperature such that the thermal diffusivity, $\chi(\mathbf{x}, t) = K(\mathbf{x}, t)/c_P \rho(\mathbf{x}, t)$, varies several orders of magnitude as function of height (e.g. K  p  l   2019b). Thus it is numerically desirable to introduce subgrid-scale (SGS) entropy diffusion that does not contribute to the net energy transport, but which damps fluctuations near grid scale. This is implemented via an SGS entropy flux (e.g. Rogachevskii & Kleeorin 2015)

$$F_{\text{SGS}} = -\chi_{\text{SGS}}^{(1)} \rho \nabla s', \quad (11)$$

where

$$s' = s - \langle s \rangle_t, \quad (12)$$

is the fluctuation of the entropy, and where $\langle s \rangle_t(\mathbf{x}, t)$ is a running temporal mean of the specific entropy with an averaging time interval of roughly 75 days. This differs from commonly adopted SGS models in that the fluctuation that the SGS term acts on, Equation (12), is not based on a difference to a spatial average (e.g. K  p  l   et al. 2020), or to a fixed reference state (e.g. Browning 2008; Gastine et al. 2012). This choice has a physical and computational justification: spatially averaged means practically always assume certain symmetries of the solution (for example, spherical or axisymmetry) but even the actual mean state might not have these symmetries if, for example, a strong low- m non-axisymmetric magnetic field is present. Furthermore, time averaging is computationally advantageous because no global

communication is not required. However, a caveat is that if the entropy field acquires numerical artifacts they will also propagate to \bar{s}_t . This was encountered in a few cases where hyperdiffusion proportional to $\nabla^6 \langle s \rangle_t$ was applied to ensure the smoothness of the time average.

The heating term \mathcal{H} is a parameterization of nuclear energy production in the core of the star and it is given by a normalized Gaussian profile

$$\mathcal{H}(r) = \frac{L_{\text{sim}}}{(2\pi w_L^2)^{3/2}} \exp\left(-\frac{r^2}{2w_L^2}\right), \quad (13)$$

where L_{sim} is the imposed luminosity in the simulation and $w_L = 0.162R$ is the width of the Gaussian, see Fig. 1 of Dobler et al. (2006).

Finally, the term \mathcal{C} in the entropy equation models radiative losses above the stellar surface with a cooling term

$$\mathcal{C}(\mathbf{x}) = \rho c_P \frac{T(\mathbf{x}) - T_{\text{surf}}}{\tau_{\text{cool}}} f_e(r), \quad (14)$$

where $\tau_{\text{cool}} = \tau_{\text{damp}}$ is a cooling timescale, and f_e is the same function as in Eq. (8) with $r_{\text{cool}} = r_{\text{damp}}$ and $w_{\text{cool}} = w_{\text{damp}}$.

2.1. Simulation strategy, units, and control parameters

The use of fully compressible formulation of the MHD equations means that using realistic stellar parameters leads to prohibitively long Kelvin–Helmholtz timescale $\tau_{\text{KH}} = GM^2/RL$, where L is the luminosity of the star, and a short time step (in comparison to the advective time) due to the low Mach number. This is addressed by using a much higher luminosity in the models than in the real star. This is described by the luminosity ratio $L_{\text{ratio}} = L_{\text{sim}}/L$ between the simulation and the star. The enhanced luminosity leads to convective velocity enhancement according to $u_{\text{conv}} \propto L_{\text{ratio}}^{1/3}$. However, it is advantageous to reinterpret the convective velocities produced in the simulation as the physical velocity. This entails re-scaling the sound speed c_s (temperature) proportional to $L_{\text{ratio}}^{-1/3}$ ($L_{\text{ratio}}^{-2/3}$). Furthermore, the Kelvin–Helmholtz time scales as $\tau_{\text{KH}} \propto L_{\text{ratio}}^{-1}$. This implies that the acoustic timestep δt_{ac} increases proportional $L_{\text{ratio}}^{1/3}$ and the gap between δt_{ac} and τ_{KH} reduces by a cumulative factor $L_{\text{ratio}}^{4/3}$. This procedure enables τ_{KH} to be resolved given that L_{ratio} is sufficiently large. The main effect of this is that the Mach number and relative fluctuations of thermodynamic quantities are enhanced which, however, scale with known power laws as functions of L_{ratio} (K  p  l   et al. 2020). The main physical difference is that overshooting at the interfaces of radiative and convective layers is also enhanced. Recent numerical experiments suggest that the enhancement of overshooting is much weaker than that of the convective velocities (K  p  l   2019b). This aspect is, however, unimportant in the fully convective setups considered here.

The units of length, time, density, entropy, and magnetic field are

$$[x] = R, \quad [t] = \sqrt{R^3/GM}, \quad [\rho] = \rho_0, \quad (15)$$

$$[s] = c_P, \quad [B] = \sqrt{\mu_0 \rho_0} [x]/[t], \quad (16)$$

where ρ_0 is the initial value of the density at the centre of the star. The results are often quoted in physical units such that the quantities on the rhs of Equations (15) and (16) use values from literature (see below).

The following input parameters define the models. The dimensionless luminosity \mathcal{L} is given by (Dobler et al. 2006)

$$\mathcal{L} = \frac{L_{\text{sim}}}{\sqrt{G^3 M^5 / R^5}}, \quad (17)$$

where $\mathcal{L} = 5.5 \cdot 10^{-5}$ for the runs discussed in the present study. This is three orders of magnitude smaller than in Dobler et al. (2006) but still much higher than in an main-sequence M5 dwarf. The amount of density stratification is determined by the dimensionless pressure scale height at the surface

$$\xi_0 = \frac{RT_{\text{surf}}}{GM/R}, \quad (18)$$

where $T_{\text{surf}} = T(R)$. The current simulations have $\xi_0 \approx 0.062$ which results in an initial density contrast of roughly 50 which is an order of magnitude greater than in the simulations of Dobler et al. (2006).

Stellar parameters for an M5 dwarf used by Dobler et al. (2006) are $M = 0.21M_{\odot}$, $R = 0.27R_{\odot}$, $L = 0.008L_{\odot}$ and $T_{\text{eff}} = 4000$ K. Therefore, $\mathcal{L}_{\text{M5}} = 2.4 \cdot 10^{-14}$ and $\xi_{\text{M5}} = 2.2 \cdot 10^{-4}$. Thus the simulations have a much higher luminosity and lower density stratification than in reality. With $\mathcal{L} = 5.5 \cdot 10^{-5}$ the luminosity ratio between the simulation and an M5 star is $L_{\text{ratio}} = \mathcal{L}/\mathcal{L}_{\text{M5}} \approx 2.1 \cdot 10^9$. Thus the velocities are greater by a factor $L_{\text{ratio}}^{1/3} \approx 1280$ such that the rotation rate of the star needs to be enhanced by the same factor to model a realistic rotational influence on the flow. This means that the centrifugal force would be unrealistically large in comparison to the acceleration due to gravity if it were explicitly included (see Käpylä et al. 2020).

The surface gravity for the M5 star is

$$g = \frac{GM}{R^2} = \frac{0.21}{(0.27)^2} \frac{GM_{\odot}}{R_{\odot}^2} \approx 2.9g_{\odot} \approx 750 \frac{\text{m}}{\text{s}^2}, \quad (19)$$

where $g_{\odot} = 260 \text{ m s}^{-2}$. Thus the conversion factor between the rotation rate in the simulations and physical units is (cf. Appendix A of Käpylä et al. 2020)

$$\Omega^{\text{sim}} = L_{\text{ratio}}^{1/3} \left(\frac{g^{\text{sim}}}{g} \frac{R}{R_{\text{sim}}} \right)^{1/2} \Omega, \quad (20)$$

where g , R , Ω are the surface gravity, stellar radius, and rotation rate in physical units and quantities with superscript ‘sim’ in simulation (code) units. For example, assuming an M5 star rotating at the solar rotation rate $\Omega_{\odot} = 2.7 \cdot 10^{-6} \text{ s}^{-1}$ yields

$$\Omega_{\odot}^{\text{sim}} = 1.73 \left(\frac{g^{\text{sim}}}{R_{\text{sim}}} \right)^{1/2}. \quad (21)$$

Rotation rates corresponding to rotation periods $P_{\text{rot}} = 2\pi/\Omega_0$ between 4.3 and 430 days are considered in the present study.

The Taylor number is given by

$$\text{Ta} = \frac{4\Omega_0^2 R^4}{\nu^2}. \quad (22)$$

The remaining control parameters are the SGS and magnetic Prandtl numbers

$$\text{Pr}_{\text{SGS}} = \frac{\nu}{\chi_{\text{SGS}}^{(1)}}, \quad \text{Pm} = \frac{\nu}{\eta}. \quad (23)$$

In the current study $\text{Pr}_{\text{SGS}} = 0.2$ and $\text{Pm} = 0.5$ are used throughout. The radiative diffusion $\chi = K/\rho c_{\text{P}} \ll \chi_{\text{SGS}}^{(1)}$ in

the cases considered here such that the corresponding Prandtl number is $\gg 1$, see Table 1.

Impenetrable and stress-free boundary conditions are imposed for the flow and the magnetic field is assumed to be perpendicular to the boundary. The thermodynamic quantities are assumed to have vanishing gradients at the edges of the box.

The simulations were run with the PENCIL CODE¹ which is a high-order finite-difference code for solving ordinary and partial differential equations (Brandenburg et al. 2020).

2.2. Diagnostics quantities

The hydrostatic non-convecting solution of Equations (2) to (4) has only a very thin convectively unstable layer near the surface Brandenburg (2016) due to the strong temperature and density dependence of the heat conductivity from the Kramers’ law. Thus the Rayleigh number is quoted from the statistically steady states of the simulations and defined as

$$\text{Ra}_{\text{t}} = \frac{g_{\text{m}} R^4}{\nu \chi_{\text{SGS}}^{(1)}} \left(-\frac{1}{c_{\text{P}}} \frac{d\langle s \rangle_{\theta\phi t}}{dr} \right)_{\text{m}}, \quad (24)$$

where the subscript m and $\langle \cdot \rangle_{\theta\phi t}$ refer to evaluating quantities at $r = 0.5R$ and to horizontal and temporal averaging, respectively. As shown in Käpylä (2019b), the SGS entropy diffusion $\chi_{\text{SGS}}^{(1)}$ is the dominant contributor to the convective stability measured by the Rayleigh number.

The rotational influence on the flow is measured by the Coriolis number

$$\text{Co} = \frac{2\Omega_0}{u_{\text{rms}} k_R}, \quad (25)$$

where Ω_0 is the rotation rate of the star, u_{rms} is the volume averaged rms velocity within a spherical radius $r < R$, and where $k_R = 2\pi/R$ corresponds to the scale of the largest convective eddies. To facilitate comparisons to other studies (e.g. Browning 2008; Brown et al. 2020) an alternative vorticity-based formulation

$$\text{Co}^{(\omega)} = \frac{2\Omega_0}{\omega_{\text{rms}}} \quad (26)$$

is also used, where ω_{rms} is the volume averaged rms vorticity $\omega = \nabla \times \mathbf{U}$ within $r < R$. Rossby numbers corresponding to the Coriolis numbers is given by $\text{Ro} = \text{Co}^{-1}$.

The fluid and magnetic Reynolds numbers are defined as

$$\text{Re} = \frac{u_{\text{rms}}}{\nu k_R}, \quad \text{Re}_{\text{M}} = \frac{u_{\text{rms}}}{\eta k_R}, \quad (27)$$

and the SGS Péclet number is given by

$$\text{Pe} = \frac{u_{\text{rms}}}{\chi_{\text{SGS}}^{(1)} k_R}. \quad (28)$$

Mean quantities are considered to be azimuthal averages (in cylindrical coordinates):

$$\bar{f}(\varpi, z, t) = \frac{1}{2\pi} \int f(\varpi, \phi, z) d\phi, \quad (29)$$

where $\varpi = r \sin \theta$ is the cylindrical radius. Temporal averages over the statistically stationary state are often additionally applied. Most of the averaged results are presented in cylindrical coordinates (ϖ, z) but in some cases it is more relevant to discuss vector quantities transformed to spherical polar coordinates (r, θ, ϕ) . Such quantities are marked with additional superscript sph, for example, \mathbf{U}^{sph} .

¹ <https://github.com/pencil-code/>

Table 1. Summary of the runs.

Run	$P_{\text{rot}}[\text{days}]$	$T_{\text{a}}[10^8]$	$u_{\text{rms}}[\text{m/s}]$	$B_{\text{rms}}[\text{kG}]$	Co	$\text{Co}^{(\omega)}$	Ra_t	Re	Pe	Re_M	$\tau_{\text{sim}}[\text{years}]$	DR
HD1	—	—	18	—	—	—	$9.1 \cdot 10^5$	189	37	—	302	—
RHD1	433	0.16	17	—	0.6	0.1	$3.2 \cdot 10^6$	181	36	—	58	anti-solar
RHD2	144	1.4	15	—	1.9	0.2	$2.5 \cdot 10^6$	159	31	—	37	solar-like
RHD3	43	16	15	—	6.4	0.9	$6.1 \cdot 10^6$	159	31	—	36	solar-like
RHD4	14	144	9.0	—	31	3.0	$1.6 \cdot 10^7$	96	19	—	220	solar-like
RHD5	4.3	1600	5.7	—	166	11	$1.0 \cdot 10^8$	61	12	—	209	solar-like
MHD1	433	0.16	14	1.3	0.7	0.1	$1.6 \cdot 10^6$	145	29	72	143	anti-solar
MHD2	144	1.4	14	0.5	2.0	0.3	$2.4 \cdot 10^6$	152	30	76	107	solar-like
MHD3	43	16	10	1.2	9.1	1.2	$4.3 \cdot 10^6$	111	22	55	134	solar-like
MHD4	14	144	5.8	1.5	49	3.6	$1.2 \cdot 10^7$	62	12	31	201	solar-like
MHD5	4.3	2500	2.6	2.2	366	24	$1.5 \cdot 10^7$	34	6	17	302	solar-like

Notes. All simulations have $\mathcal{L} = 5.5 \cdot 10^5$ and a grid resolution of 288^3 . The diffusion coefficients are $\nu = 2.8 \cdot 10^6 \text{ m}^2/\text{s}$, $\chi_{\text{SGS}}^{(1)} = 1.4 \cdot 10^7 \text{ m}^2/\text{s}$, and $\eta = 5.6 \cdot 10^6 \text{ m}^2/\text{s}$, in all cases except in run MHD5 where $\nu = 2.2 \cdot 10^6 \text{ m}^2/\text{s}$, $\chi_{\text{SGS}}^{(1)} = 1.1 \cdot 10^7 \text{ m}^2/\text{s}$, and $\eta = 4.4 \cdot 10^6 \text{ m}^2/\text{s}$. The initial value of $\chi = 2.0 \cdot 10^3 \text{ m}^2/\text{s}$ at the centre of the star. τ_{sim} is the length of the statistically steady part of the simulations and the last column indicates the sense of the differential rotation (DR).

3. Results

Three sets of simulations were made. In the first set (HD) a single purely hydrodynamic simulation HD1 without rotation was made. In the second set (RHD), rotation is included with all other parameters unchanged using thermodynamically equilibrated snapshot from run HD1. Five rotation rates were explored in the models RHD[1-5]. The final set of simulations (MHD[1-5]) were branched off from the corresponding RHD runs with additional weak random seed magnetic fields. The runs and a number of diagnostics are listed in Table 1.

3.1. Description of convective states

Representative flows and convection patterns from runs HD1 and RHD[1-5] are shown in Fig. 1. The non-rotating run HD1 shows a large-scale dipolar convection cell which fills essentially the whole star. This is similar to patterns seen in simulations of slowly rotating red giant stars which have a deep convective envelope (Brun & Palacios 2009). Rotation destroys the dipolar convection cell but the flows continue to be predominantly large scale for runs RHD1 and RHD2 with Coriolis numbers 0.6 and 1.9, respectively. For more rapid rotation the convection cells begin to show clearer rotational alignment and the horizontal size of the flow structures decreases, see the lower row of Fig. 1. This is particularly clear in the two most rapidly rotating cases RHD4 and RHD5, where the flows are dominated by helical convection columns that pierce the whole star. In the hydrodynamic run RHD5, a strong axial jet develops. This feature is not present in the corresponding magnetohydrodynamic run MHD5, see Fig. 2. In the other cases the differences between hydrodynamic and magnetohydrodynamic runs are less drastic such the flow patterns are qualitatively unchanged. The velocities are, however, in general lower in the MHD cases, see the 4th column of Table 1. Small scale convection near the surface of the star (e.g. Hotta et al. 2015) is not captured in the current simulations because of the modest density stratification in comparison to real stars.

The statistically stationary horizontally averaged thermodynamic state from the non-rotating run HD1 is shown in Fig. 3(a). The temperature varies by an order of magnitude within the star whereas the density varies by a factor of roughly 20. This cor-

responds to roughly five pressure or three density scale heights, respectively. In the nearly isothermal exterior the temperature is almost constant and the density decreases there exponentially as a function of radius. In comparison to other similar studies, the density contrast in the current simulations is thus somewhat greater than in Dobler et al. (2006), comparable to that in Brown et al. (2020), and smaller by a factor of a few in comparison to Browning (2008) and Yadav et al. (2015a, 2016).

Panel (b) of Fig. 3 shows a scatter plot of the temporally and azimuthally averaged specific entropy $\bar{s}(\varpi, z)/c_P$. Remarkably, the mean entropy decreases toward the centre of the star below $r \lesssim 70 \text{ Mm}$. Thus roughly 30 per cent of the core of the star is stably stratified according to the Schwarzschild criterion although the whole star is continuously mixed by vigorous convection. Similar configurations have recently been discussed in other contexts where the star has a clearly defined radiative core (e.g. Tremblay et al. 2015; K  p  l   et al. 2017b; Bekki et al. 2017; K  p  l   et al. 2019). Such formally stable, yet convecting, regions arise due to a non-local non-gradient contribution to the heat flux (Deardorff 1961, 1966). These regions are referred to as Deardorff zones (see, e.g. Brandenburg 2016; K  p  l   et al. 2017b). The significance of Deardorff zones in fully convective stars is that they can have an impact for the large-scale dynamos in that the magnetic fields in the possibly weakly stably stratified core are less susceptible to be buoyant.

Figure 3(b) shows further that in run MHD1 the convective layer is unstably stratified throughout whereas in run MHD3 the Deardorff layer reappears. The behavior of run MHD1 is puzzling and possibly related to the strong anti-solar differential rotation developing in that run. In the most rapidly rotating case, MHD5, the stratification is again unstable throughout. This can be understood in terms of an increasing critical Rayleigh number as the rotation increases such that a steeper temperature gradient is needed to drive convection (e.g. Chandrasekhar 1961). The current simulations were made with rather modest Rayleigh numbers and the effects of rotation are likely to be much weaker in real stars where the Rayleigh numbers are more than ten orders of magnitude greater. Figure 3(b) also shows that the latitudinal variation of mean specific entropy increases as a function of rotation indicated by the larger scatter around the horizontally averaged means.

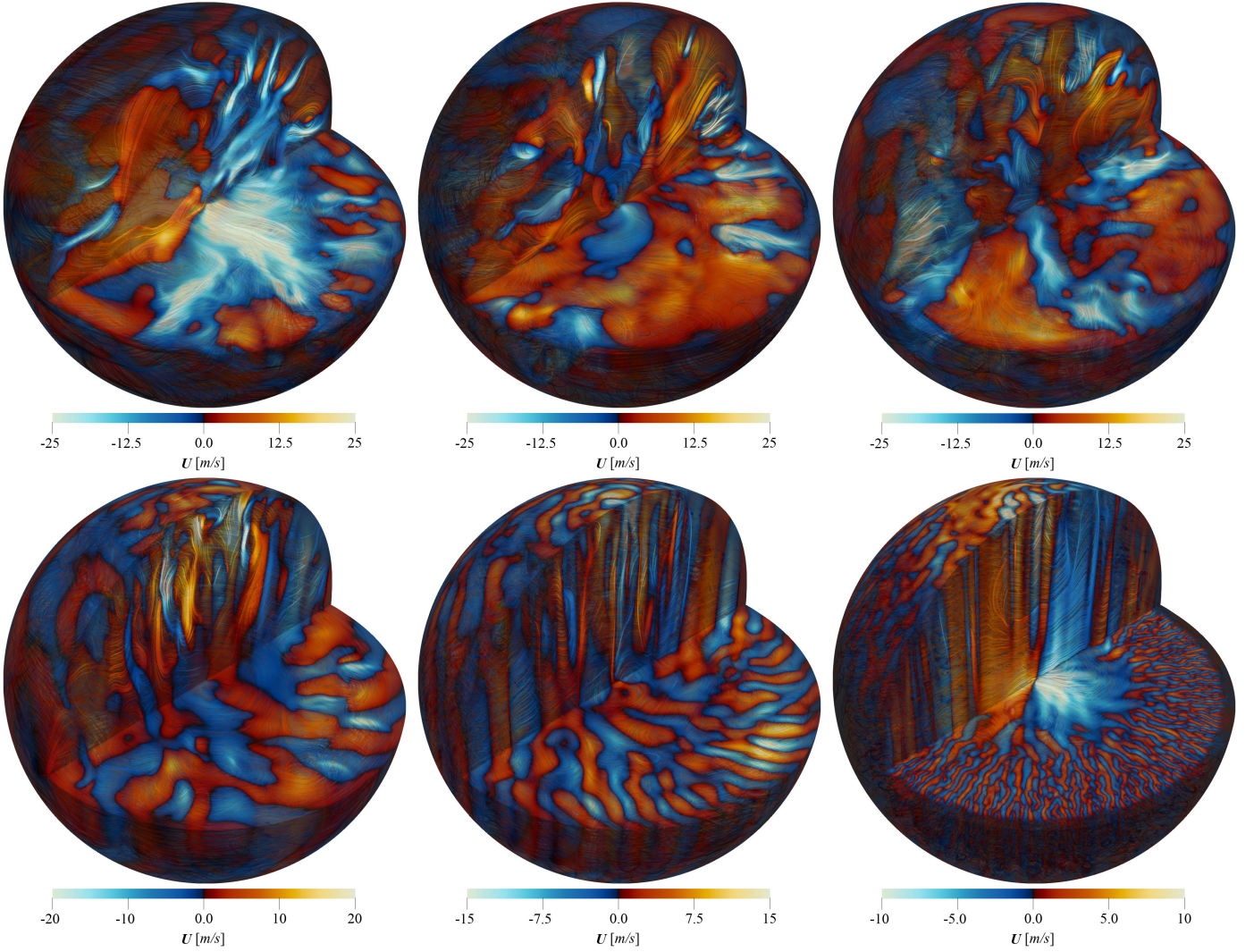


Fig. 1. Velocity fields U^{sph} in the Runs HD1, RHD1, RHD2 (top row from left to right), and RHD3, RHD4, and RHD5 (bottom row). The colour contours indicate radial velocity U_r^{sph} and the streamlines are colour-coded according to the local value of U_r^{sph} .

The luminosities related to the radiative, enthalpy, kinetic energy, cooling and heating fluxes are given by

$$\bar{L}_{\text{rad}} = -4\pi r^2 \langle K \rangle_{\theta\phi t} \frac{\partial \langle T \rangle_{\theta\phi t}}{\partial r}, \quad (30)$$

$$\bar{L}_{\text{enth}} = 4\pi r^2 c_P \langle (\rho U_r^{\text{sph}})' T' \rangle_{\theta\phi t}, \quad (31)$$

$$\bar{L}_{\text{kin}} = 2\pi r^2 \langle \rho U^2 U_r^{\text{sph}} \rangle_{\theta\phi t}, \quad (32)$$

$$\bar{L}_{\text{visc}} = -8\pi r^2 \nu \langle \rho U_i^{\text{sph}} S_{ir}^{\text{sph}} \rangle_{\theta\phi t}, \quad (33)$$

$$\bar{L}_{\text{cool}} = - \int_0^r 4\pi r^2 \langle \mathcal{C} \rangle_{\theta\phi t} dr, \quad (34)$$

$$\bar{L}_{\text{heat}} = \int_0^r 4\pi r^2 \langle \mathcal{H} \rangle_{\theta\phi t} dr, \quad (35)$$

where the primes indicate fluctuations from from an azimuthally averaged mean. Furthermore, the total convected luminosity is the sum of the enthalpy and kinetic energy luminosities (Cattaneo et al. 1991)

$$\bar{L}_{\text{conv}} = \bar{L}_{\text{enth}} + \bar{L}_{\text{kin}}. \quad (36)$$

The luminosities from Equations (30) and (35) from the non-rotating hydrodynamic run HD1 are shown in Fig. 4. The luminosities due to viscous and radiative fluxes are less than one per

cent of the total everywhere and they are not shown. The radiative flux is likely underestimated in the current simulations due to a value of K_0 that is smaller than that corresponding to an M5 dwarf in ELM. However, the effect of this for the resulting flows and dynamos is likely to be weak. The dominant components are due to the outward enthalpy flux (\bar{L}_{enth}) and the inward kinetic energy flux (\bar{L}_{kin}). The maximum value of the latter is close to the stellar luminosity which is compensated by a correspondingly higher flux of enthalpy such that the total convected luminosity matches the luminosity of the star everywhere except near the surface where the cooling is effective. In the rotating cases the enthalpy and kinetic energy luminosity contributions decrease while they still transport the majority of the flux, similarly as in the fully convective models of Brown et al. (2020).

3.2. Large-scale flows

The density-stratified and rotating convective envelopes of fully convective stars have all the ingredients for generating large-scale mean flows via the Λ effect (e.g. Rüdiger 1980, 1989; Käpylä 2019a). The ensuing differential rotation and meridional circulation are of prime importance for large-scale dynamos. Simulations in spherical shells indicate that two qualitatively dif-

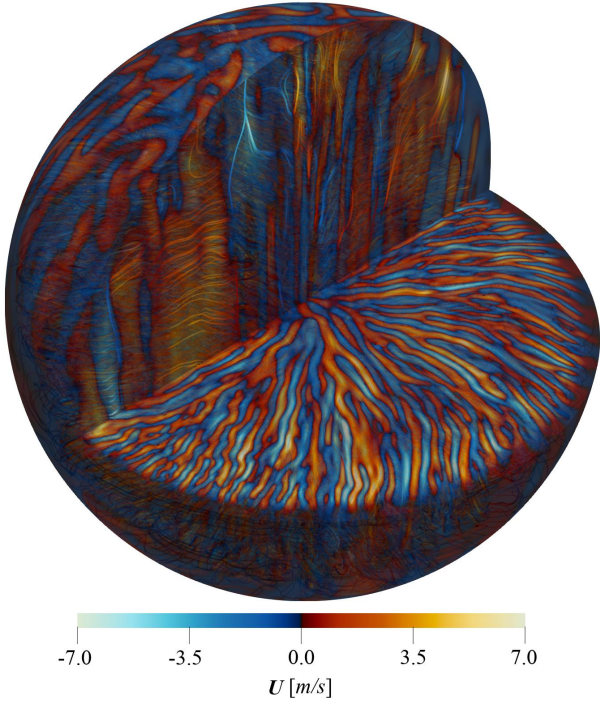


Fig. 2. Same as Fig. 1 but for run MHD5.

Table 2. Differential rotation parameters.

Run	$\Delta_{\Omega}^{(r)}$	$\Delta_{\Omega}^{(\bar{\theta})}(60^\circ)$	$\Delta_{\Omega}^{(\bar{\theta})}(75^\circ)$
RHD1	-6.56	-1.18	-2.75
RHD2	0.15	0.24	0.45
RHD3	0.30	0.15	0.30
RHD4	0.087	0.018	0.050
RHD5	$-1.2 \cdot 10^{-3}$	$2.6 \cdot 10^{-3}$	$-5.8 \cdot 10^{-3}$
MHD1	-2.96	-0.89	-1.99
MHD2	0.13	0.19	0.37
MHD3	0.15	0.064	0.16
MHD4	$1.1 \cdot 10^{-3}$	$7.5 \cdot 10^{-3}$	$4.2 \cdot 10^{-4}$
MHD5	$-8.3 \cdot 10^{-5}$	$3.0 \cdot 10^{-4}$	$1.7 \cdot 10^{-4}$

Notes. The numbers are computed from temporally and azimuthally averaged angular velocity $\bar{\Omega}(r, \theta)$ with Equations (39) and (40) for each run.

ferent flow regimes exist depending on the Coriolis number. For slow rotation the differential rotation is anti-solar, such that the equatorial rotation rate is slower than the polar one, whereas for rapid rotation a solar-like rotation profile with equatorial acceleration is obtained (e.g. Gilman 1977; Aurnou et al. 2007; Käpylä et al. 2011; Guerrero et al. 2013; Gastine et al. 2014). The watershed value of the Coriolis number in such simulations is close to unity (e.g. Gastine et al. 2014).

The averaged rotation rate is given by

$$\bar{\Omega}(\varpi, z) = \Omega_0 + \bar{U}_\phi(\varpi, z)/\varpi. \quad (37)$$

Similarly, the averaged meridional flow is given by

$$\bar{\mathbf{U}}_{\text{mer}}(\varpi, z) = (\bar{\mathbf{U}}_\varpi, 0, \bar{U}_z), \quad (38)$$

where the velocities correspond to those in cylindrical coordinates. Both $\bar{\Omega}$ and $\bar{\mathbf{U}}_{\text{mer}}$ are averaged in time over the statistically steady part of the simulations. The averaging period are

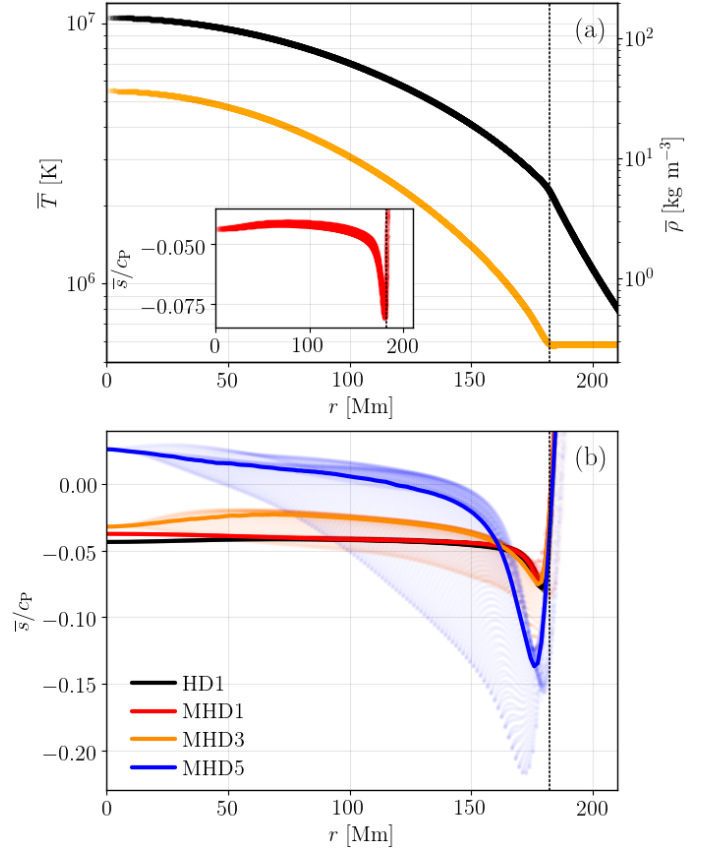


Fig. 3. Top panel: Time-averaged radial profiles of azimuthally averaged temperature \bar{T} (orange, left axis) and density $\bar{\rho}$ (black, right axis) as functions of radius from the non-rotating run HD1. The inset shows the radial profile of the mean specific entropy \bar{s}/c_p . Bottom: mean specific entropy $\bar{s}/c_p(r)$ from Runs HD1, MHD1, MHD3, and MHD5 as indicated by the legend. The dots show a scatter plot of $\bar{s}(\varpi, \theta)$ as a function of spherical radius r . The dotted vertical line indicates the upper boundary of the convective layer in the non-rotating run HD1.

listed in the 12th column of Table 1. The amplitude of the differential rotation is measured by the differential rotation parameters (e.g. Käpylä et al. 2013):

$$\Delta_{\Omega}^{(r)} = \frac{\bar{\Omega}(r_{\text{top}}, \theta_{\text{eq}}) - \bar{\Omega}(r_{\text{bot}}, \theta_{\text{eq}})}{\bar{\Omega}(r_{\text{top}}, \theta_{\text{eq}})}, \quad (39)$$

$$\Delta_{\Omega}^{(\bar{\theta})}(\theta) = \frac{\bar{\Omega}(r_{\text{top}}, \theta_{\text{eq}}) - \bar{\Omega}(r_{\text{top}}, \bar{\theta})}{\bar{\Omega}(r_{\text{top}}, \theta_{\text{eq}})}, \quad (40)$$

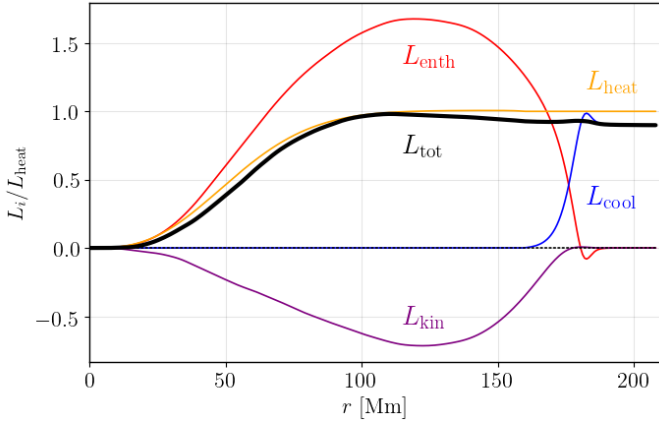
where $r_{\text{top}} = 0.9R$, $r_{\text{bot}} = 0.1R$, $\theta_{\text{eq}} = 0^\circ$ corresponds to the equator, and $\bar{\theta}$ refers to an average of $\bar{\Omega}$ from latitudes $+\theta$ and $-\theta$. Table 2 summarizes the results for $\Delta_{\Omega}^{(r)}$ and $\Delta_{\Omega}^{(\bar{\theta})}$ with $\theta = 60^\circ$ and 75° . The reason not to use the surface values for measuring the differential rotation is that the value at $r = R$ is affected by the damping of velocities in the exterior. Similarly, the values near the axis are the most uncertain and thus off-axis and off-pole values for $\Delta_{\Omega}^{(r)}$ and $\Delta_{\Omega}^{(\bar{\theta})}$ are used.

Figure 5 shows the rotation profiles of the runs in the set MHD. The case with the slowest rotation (MHD1), with $P_{\text{rot}} = 433$ days and $\text{Co} = 0.7$, shows anti-solar differential rotation. This is described by negative values of $\Delta_{\Omega}^{(r)}$ and $\Delta_{\Omega}^{(\bar{\theta})}$, see the 6th row of Table 2. The anti-solar rotation profile is associ-

Table 3. Volume and time-averaged kinetic and magnetic energy densities.

Run	$E_{\text{kin}} [\text{J/m}^3]$	$E_{\text{kin}}^{\text{DR}}/E_{\text{kin}}$	$E_{\text{kin}}^{\text{MC}}/E_{\text{kin}}$	$E_{\text{mag}} [\text{J/m}^3]$	$E_{\text{mag}}/E_{\text{kin}}$	$E_{\text{mag}}^{\text{tor}}/E_{\text{mag}}$	$E_{\text{mag}}^{\text{pol}}/E_{\text{mag}}$
HD1	7134	0.047	0.200	—	—	—	—
RHD1	6834	0.519	0.040	—	—	—	—
RHD2	2153	0.179	0.045	—	—	—	—
RHD3	3542	0.640	0.019	—	—	—	—
RHD4	1548	0.579	0.024	—	—	—	—
RHD5	1144	0.127	0.018	—	—	—	—
MHD1	2957	0.306	0.072	358	0.121	0.095	0.080
MHD2	1890	0.140	0.045	50	0.027	0.074	0.068
MHD3	1377	0.395	0.025	236	0.172	0.256	0.063
MHD4	301	0.117	0.014	483	1.604	0.044	0.053
MHD5	63	0.016	0.014	1112	17.528	0.017	0.039

Notes. The total kinetic energy density is $E_{\text{kin}} = \frac{1}{2} \langle \rho \mathbf{U}^2 \rangle$ where the brackets denote volume averaging within spherical radius $r \leq R$. The corresponding energy densities for the differential rotation and meridional circulation are given by $E_{\text{kin}}^{\text{DR}} = \frac{1}{2} \langle \rho \bar{U}_\phi^2 \rangle$ and $E_{\text{kin}}^{\text{MC}} = \frac{1}{2} \langle \rho (\bar{U}_\varpi^2 + \bar{U}_z^2) \rangle$, respectively. The energy densities of the total, toroidally averaged toroidal and poloidal magnetic fields are given by $E_{\text{mag}} = \langle \mathbf{B}^2 / 2\mu_0 \rangle$, $E_{\text{mag}}^{\text{tor}} = \langle \bar{B}_\phi^2 / 2\mu_0 \rangle$, and $E_{\text{mag}}^{\text{pol}} = \langle (\bar{B}_\varpi^2 + \bar{B}_z^2) / 2\mu_0 \rangle$, respectively.


Fig. 4. Contributions to the luminosity from enthalpy (red), kinetic energy (purple), cooling (blue), and heating (orange) fluxes in Run HD1.

ated with a single-cell counter-clockwise meridional flow pattern with outward flow at the equator. This is similar to runs 2b and 2c of Dobler et al. (2006), see their Fig. 11. The amplitude of the meridional flow is relatively large, about 4 m/s which corresponds to 20 per cent of the overall rms velocity. These results coincide qualitatively with simulations of thinner convective shells in spherical coordinates (e.g. Käpylä et al. 2014). In run MHD2, with $P_{\text{rot}} = 144$ days and $\text{Co} = 2.0$, the rotation profile is solar-like with positive $\Delta_\Omega^{(r)}$ and $\Delta_\Omega^{(\theta)}$, see the 7th row of Table 2. Thus the transition between anti-solar and solar-like profiles occurs in the Coriolis number range $0.7 \dots 2.0$. This is slightly lower than in spherical shell convection (e.g. Käpylä et al. 2011; Gastine et al. 2014; Viviani et al. 2018) where the transition occurs typically somewhere between $\text{Co} = 2 \dots 3$. However, due to the differences in the setups including the geometry, Prandtl numbers, spatial resolution, and Reynolds and Péclet numbers there is no reason to expect that the transition would occur at precisely at the same Co . Nevertheless, it is safe to conclude that the anti-solar to solar-like transition occurs at a similar rotational influence in fully and partially convective models.

The amplitudes of the differential rotation are the largest in the cases MHD1 and MHD2, see 6th and 7th lines of Table 2. A comparison of $\Delta_\Omega^{(r)}$ and $\Delta_\Omega^{(\theta)}$ with Fig. 5 indicates that the latter somewhat exaggerates the amplitude of the differential rotation for these runs because the highest values of $\bar{\Omega}$ in both cases occur in small regions near the axis where the accuracy of the ϕ -averages is the poorest. Nevertheless, the amplitude of the differential rotation is substantially larger in these two runs in comparison to the more rapidly rotating cases, although the fraction of the kinetic energy in the mean flows in the latter is relatively low, see the 3rd to 5th columns of Table 3. The rotation profile of the MHD2 is also asymmetric with respect to the equator. This is most likely caused by the asymmetric large-scale magnetic field configuration in that simulation (see below). Similar asymmetric large-scale flow and magnetic field configurations were reported in Dobler et al. (2006), see their Fig. 11. Furthermore, asymmetry is absent in the corresponding hydrodynamic run RHD2 (not shown). The meridional flow pattern in run MHD2 consists of four (two) cells near to (away from) the rotation axis. The meridional flow is also asymmetric near the equator with maximum flow speeds of the order of 3 m/s. Comparison between runs MHD[1-2] with corresponding hydrodynamic runs RHD[1-2] shows a reduction of differential rotation of roughly 20 per cent, except for $\Delta_\Omega^{(r)}$ in run MHD1 which is reduced by more than 50 per cent.

In run MHD3 the rotation profile is similar to that in MHD2 but no equatorial asymmetry is present, see Fig. 5. In MHD3 and the more rapidly rotating cases the maximum meridional circulation amplitudes occur outside the star and the flows within the star are significantly weaker. However, as shown in Fig. 5, the mass flux due to these exterior flows is weak due to the rapidly decreasing density for $r > R$. The values of $\Delta_\Omega^{(r)}$ and $\Delta_\Omega^{(\theta)}$ in runs MHD[2-3] are similar to those of the Sun. However, magnetic quenching of differential rotation in run MHD3 in comparison to the corresponding hydrodynamic run RHD3 is significantly stronger than for runs MHD2/RHD2. This is likely explained by the stronger magnetic fields in run MHD3 in comparison to MHD2, see the 5th column of Table 1 and Table 3.

In the two most rapidly rotating runs (MHD4 and MHD5) the amplitude of the differential rotation decreases further such that in the latter run the deviations from solid body rotation are

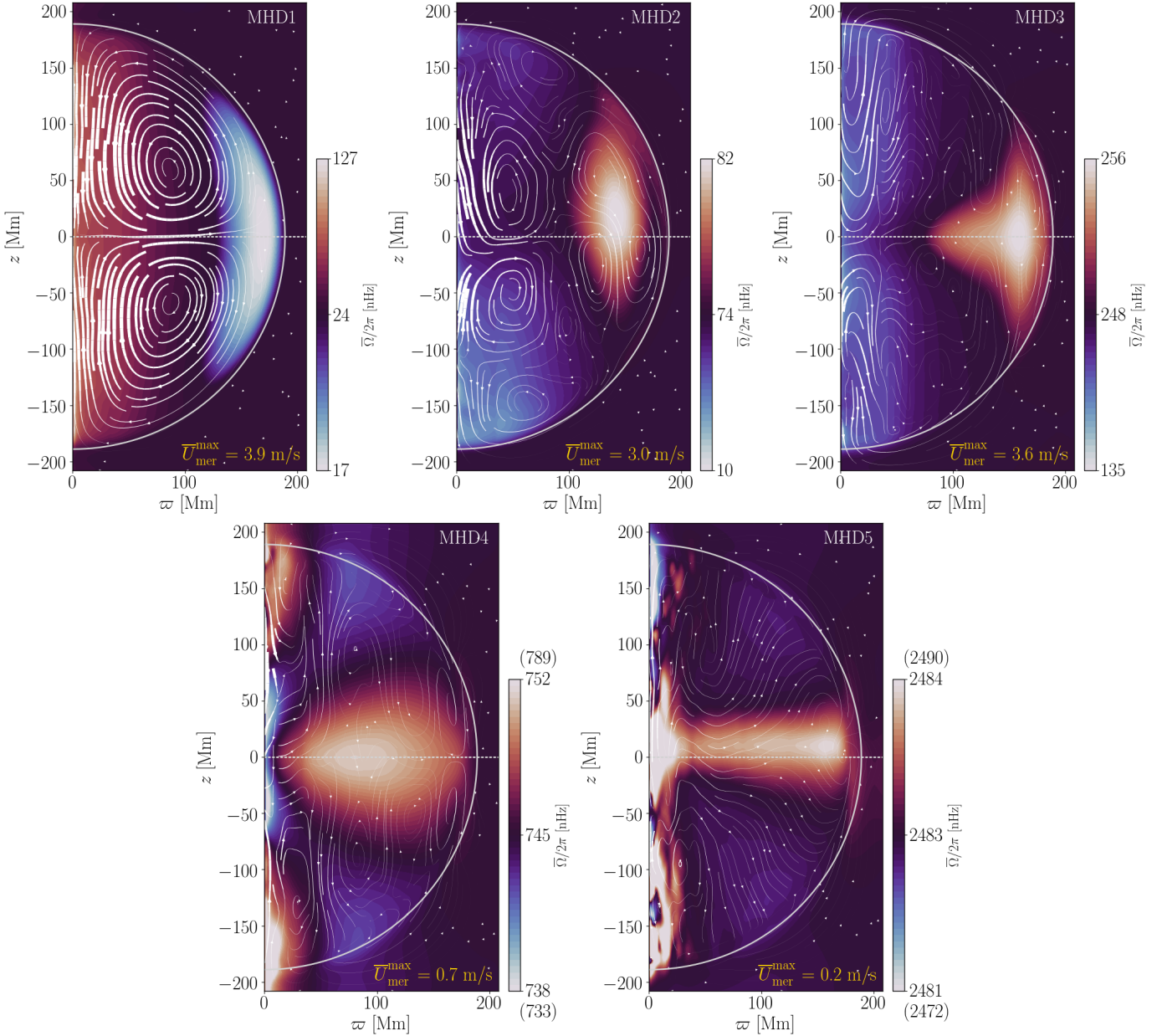


Fig. 5. Temporally and azimuthally averaged rotation profiles $\bar{\Omega}(\varpi, z)$ for the simulations in set MHD. The values for runs MHD4 and MHD5 are clipped to highlight features near the equator. The full ranges are indicated in the parenthesis above and below the colourbar. The arrows indicated the mass flux due to meridional circulation $\bar{\rho}\bar{U}_{\text{mer}}$. The arrow widths are proportional to $|\bar{\rho}\bar{U}_{\text{mer}}|$. The maximum meridional flow speeds are indicated on the lower right corners of each panel.

very small, see the lower row of Fig. 5 and the 9th and 10th rows in Table 2. The meridional flow also decreases and the largest values are always found outside of the star in both cases. The rotation profile shows axially aligned structures consistent with the Taylor–Proudman balance in run MHD3 but a similar dominance is not as clear from the mean flows in cases MHD4 and MHD5. This is possibly because the mean flows are weak in both cases such that these models are nearly in solid body rotation. This is expected because for rapid enough rotation turbulent angular momentum transport, and therefore the mean flows, are quenched such that the system approaches solid body rotation for $\Omega_0 \rightarrow \infty$ (e.g. Kichatinov & R  diger 1993; Gastine et al. 2014). However, inspection of instantaneous velocity fields reveals flow structures that are very much in line with Taylor–Proudman constraint, see Figs. 1 and 2.

The simulations reported in Dobler et al. (2006) all have anti-solar differential rotation. The Coriolis numbers were not given in that study but it is possible to calculate Co according to Equation (25) with the data presented in the paper. That is, $\text{Co} = \Omega_0 R^2 / (\nu \text{Re})$, where the relevant quantities on the rhs are listed in Table 1 of Dobler et al. (2006). The Coriolis numbers for their runs 2[b–e] are 0.9, 4.9, 18, and 47, respectively. Based on these values it is somewhat surprising that the differential rotation is anti-solar in their most rapidly rotating cases. However, the rotation profiles in Dobler et al. (2006) are shown from the saturated dynamo regime where the magnetic field has a considerable back-reaction to the flow. Furthermore, in the most rapidly rotating cases the supercriticality of convection is likely to be even weaker than in the present simulations. Thus it is plausible that the two most rapidly rotating cases (2d and 2e)

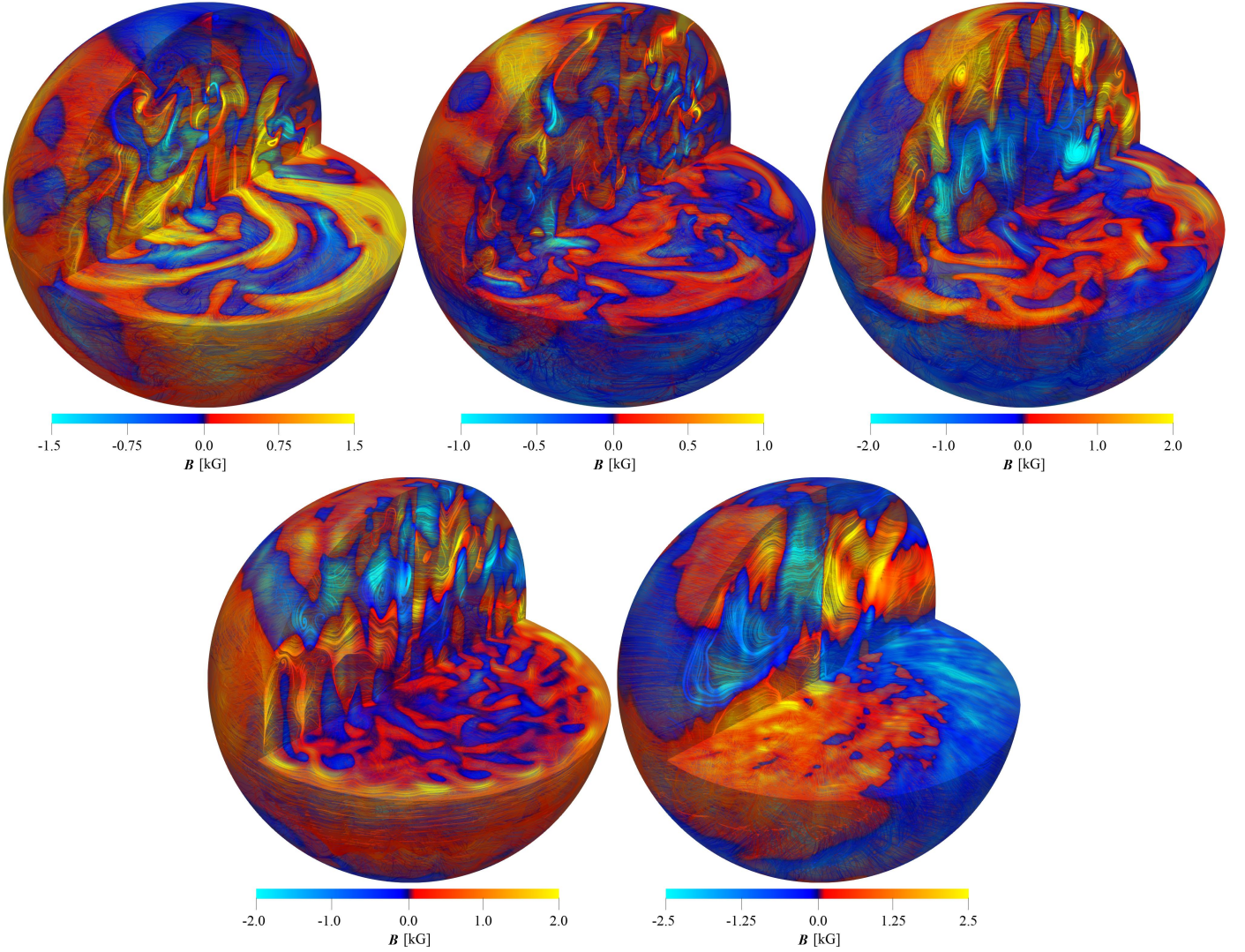


Fig. 6. Instantaneous magnetic fields B^{sph} in the Runs MHD1, MHD2, MHD3 (top row from left to right), and MHD4, and MHD5 (bottom row). The colour contours indicate radial magnetic field B_{ϕ}^{sph} and the streamlines are colour-coded according to the local value of B_{ϕ}^{sph} .

in Dobler et al. (2006) are comparable to the current runs MHD4 and MHD5 with weak differential rotation in general.

The rotation profiles of all runs with solar-like rotation profiles (MHD[2-5]) all have multiple meridional circulation cells. This is independent of magnetic fields because the corresponding hydrodynamic runs have qualitatively similar meridional flow structure. On the other hand, mean-field models of fully convective stars, relying on parameterization of turbulence in terms of turbulent viscosity and Λ effect (Pipin 2017; Pipin & Yokoi 2018) almost invariably produce a single-cell meridional circulation pattern. However, the amplitude of the differential rotation in the $P_{\text{rot}} = 10$ d model of Pipin (2017) is very close to that in Run MHD4.

3.3. Dynamo solutions

All of the rotating magnetohydrodynamic runs MHD[1-5] produce large-scale dynamos starting from a low amplitude (~ 0.1 G) random small-scale seed field. Representative instantaneous magnetic fields from each of the MHD runs are shown in Fig. 6. While the slowly rotating cases MHD[1-2] do not appear

to show large-scale order at the first glance, the more ordered large-scale structure of the magnetic field in the intermediate and rapidly rotating cases MHD[3-5] is immediately clear.

The mean field is considered to be the azimuthally averaged field $\overline{B}(r, \theta, t)$ or $\overline{B}(\varpi, z, t)$. Space-time diagrams of $\overline{B}_{\phi}(R, \theta, t)$ for a period of 100 years for each of the MHD runs are shown in Fig. 7. The model with the slowest rotation (MHD1, $P_{\text{rot}} = 430$ days) produces a quasi-stationary large-scale field without sign reversals during the simulated period. This is similar to results obtained from spherical wedges and fully spherical shells in the slowly rotating regime where differential rotation is anti-solar (Käpylä et al. 2017a; Warnecke 2018; Strugarek et al. 2018). A similar quasi-stationary solution is also obtained in case MHD2 that has solar-like differential rotation. Similar quasi-stationary configurations have been reported also from spherical shells with solar-like differential rotation (e.g. Brown et al. 2010; Guerrero et al. 2016) along with solutions with apparently random sign reversals (e.g. Fan & Fang 2014; Hotta et al. 2016). This type of solutions appears to be the norm in a parameter regime where the Coriolis number is just high enough for solar-like differential rotation to appear (e.g.

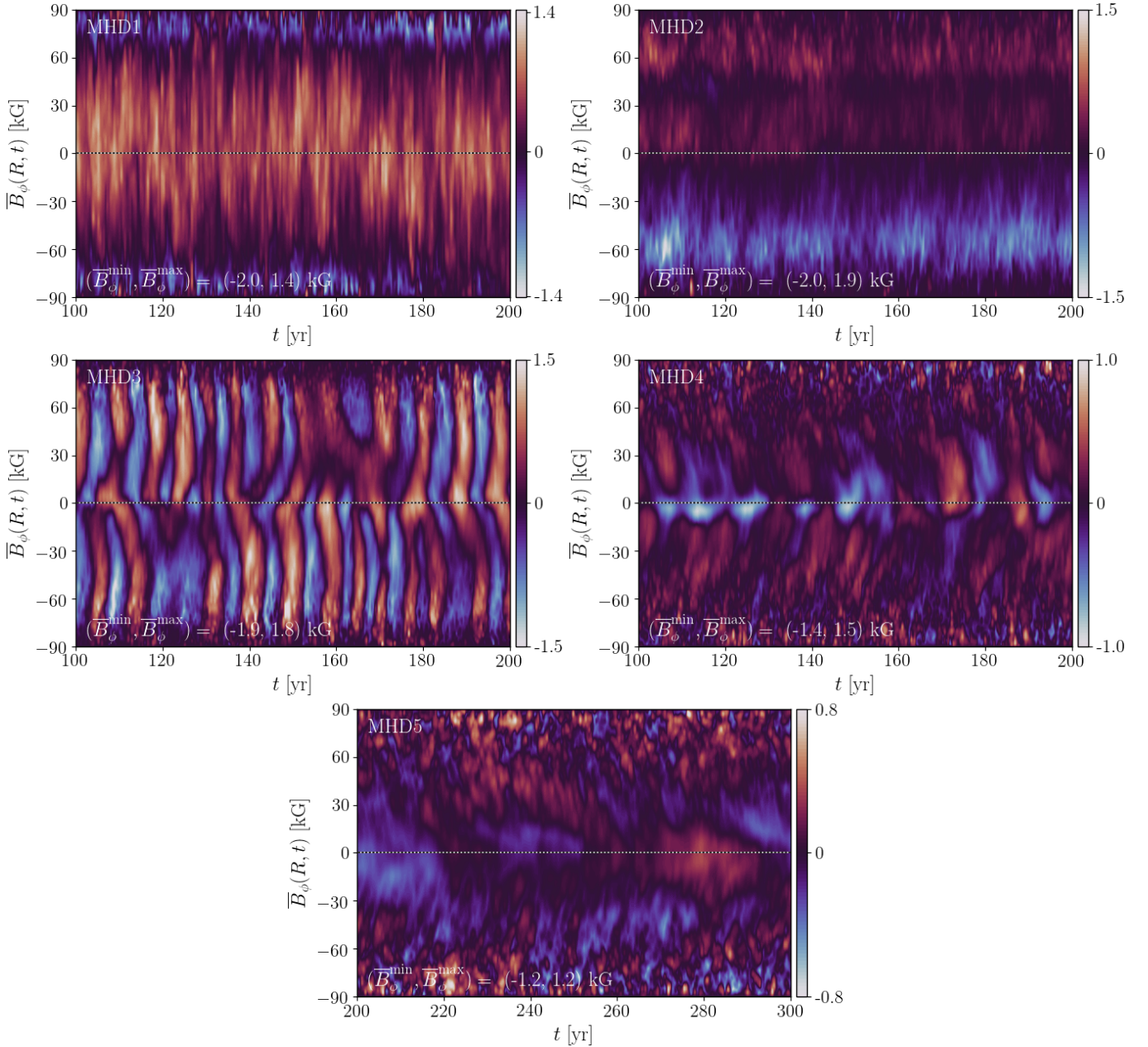


Fig. 7. Time-latitude diagrams of the mean toroidal magnetic field $\bar{B}_\phi(R, t)$ for a period of 100 yr for the MHD runs as indicated by the legends. The dotted horizontal line indicates the equator.

Warnecke 2018). Intriguingly, the kinetic helicity, $\mathcal{H} = \overline{\boldsymbol{\omega} \cdot \mathbf{U}}$, in these runs shows a profile with a mostly positive (negative) values in the upper part of the CZ in the northern (southern) hemisphere, see the left panel of Fig. 8. This is at odds with the usual argumentation for helical convective eddies in a stratified atmosphere for which $\mathcal{H} < 0$ for $\mathbf{g} \cdot \nabla \Omega < 0$.

In the intermediate rotation regime (run MHD3), with $P_{\text{rot}} = 43$ days and $\text{Co} = 9.1$, a predominantly axisymmetric and oscillatory solution is found. In this regime the rotation profile of the star is solar-like such that the radial gradient of Ω is positive almost everywhere. In combination with a mostly negative kinetic helicity on the northern hemisphere the expectation from a simple $\alpha\Omega$ dynamo is that a poleward-propagating dynamo wave appears (Parker 1955; Yoshimura 1975). This is consistent with the outcome of the simulation, see the left panel in the middle row of Fig. 7, although the region where $\mathcal{H} < 0$ is

present only near the surface of the star (middle panel of Fig. 8). However, the results for the large-scale magnetic fields are in agreement with comparable simulations in spherical shells (e.g. Gilman 1983; Käpylä et al. 2010; Brown et al. 2011; Simitev et al. 2015). The evolution of the azimuthally averaged mean magnetic field in the course of the cycle is shown in Fig. 9. The amplitude of the mean toroidal magnetic field is typically larger than the corresponding poloidal field but the difference is not particularly large, and in some instances the maximum poloidal field exceeds the maximum toroidal field. However, the volume- and time-averaged toroidal field energy is roughly four times greater than the energy of the poloidal field, see Table 3. Thus the interpretation in terms of an $\alpha\Omega$ dynamo remains plausible. However, a more detailed description, for example, in terms of mean-field modeling with turbulent transport coefficients derived from the 3D simulations with the test-field method (e.g.

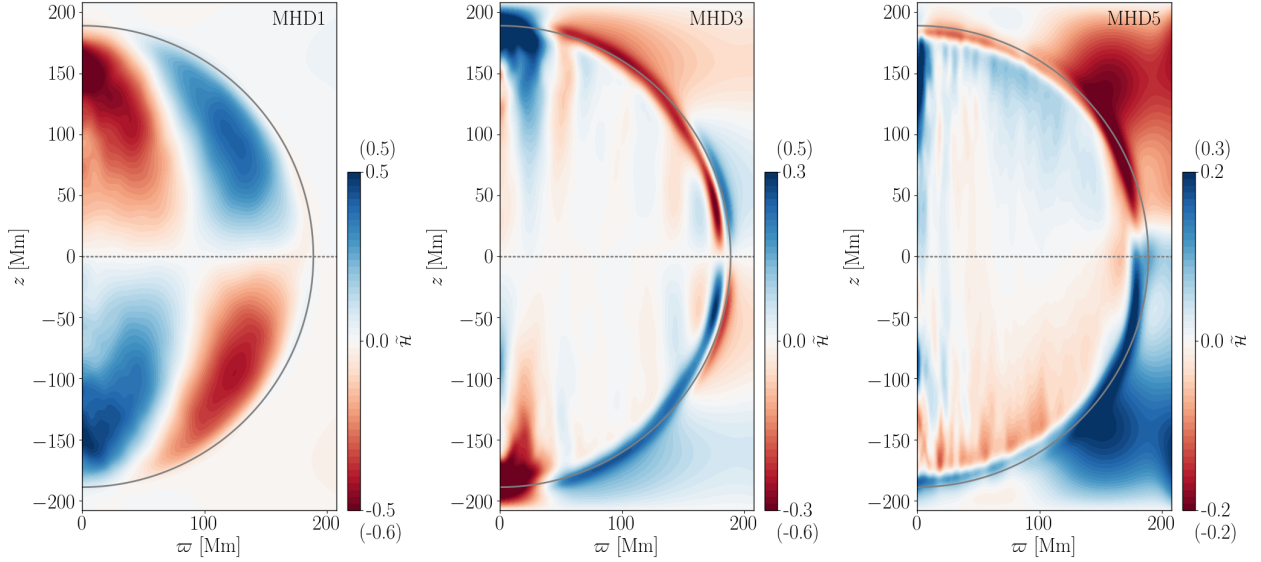


Fig. 8. Azimuthally averaged normalized kinetic helicity $\tilde{\mathcal{H}}(\varpi, z) = \mathcal{H}(\varpi, z)/u_{\text{rms}}\omega_{\text{rms}}$ for runs MHD1 (left), MHD3 (middle), and MHD5 (right). Data ranges are clipped for better legibility. The full ranges are indicated above and below the colourbars.

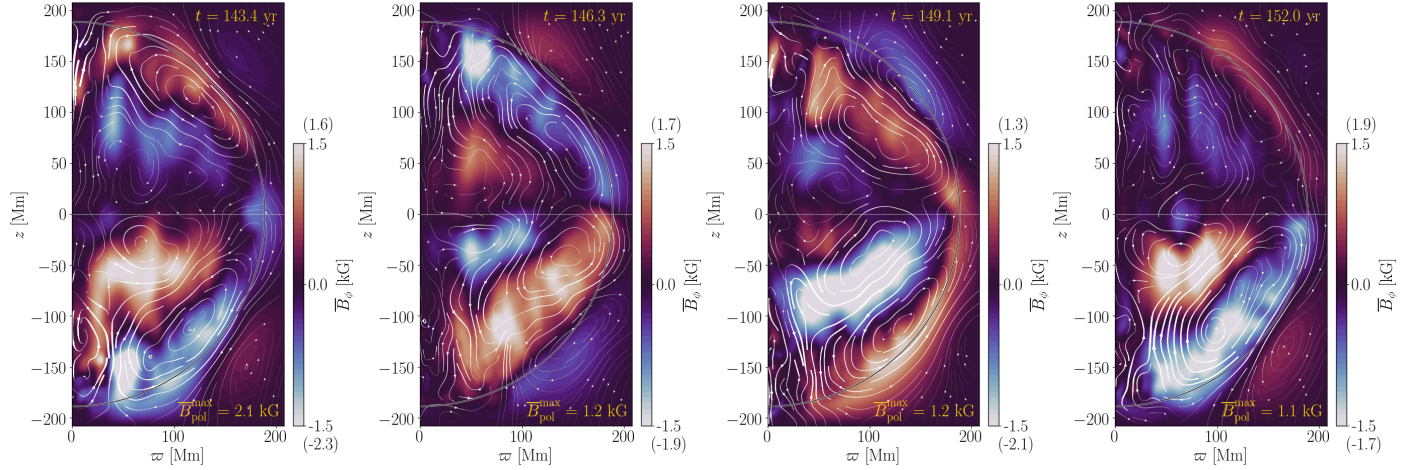


Fig. 9. Azimuthally averaged toroidal (colour contours) and poloidal (arrows) magnetic fields from four times between $t = 143.4$ and 152 years in run MHD3. The width of the arrows is proportional to the strength of the poloidal field. The values of \overline{B}_ϕ are clipped to ± 1.5 kG, and maximum and minimum values are quoted in parenthesis above and below the colourbar ranges, respectively. The amplitude of the poloidal field is indicated on the lower right corner of each panel.

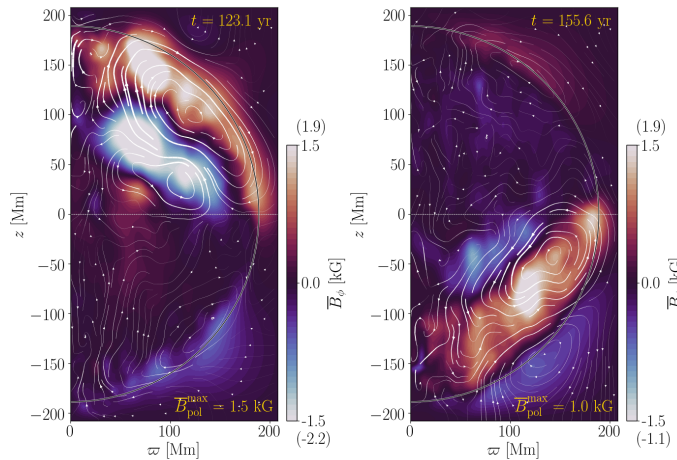


Fig. 10. Same as Fig. 9 but for $t = 123.1$ (left) and $t = 155.6$ years (right).

Schrinner et al. 2007; Warnecke et al. 2018; Warnecke & Käpylä 2020) is needed to discern the origin of the large-scale fields. This, however, is not within the scope of the present study.

In a recent study, Yadav et al. (2016) presented a spherical shell simulation extending from $r = 0.1R$ to R in a parameter regime targeting specifically the slowly rotating M dwarf Proxima Centauri with $P_{\text{rot}} \approx 90$ days. These authors found a similar poleward-propagating dynamo wave as in the current run MHD3 with a half-cycle period of roughly 9 years. The run MHD3 with $P_{\text{rot}} = 43$ days has an average half-cycle of around 4-5 years. Although the parameters of the current simulations and those of Yadav et al. (2016) do not fully overlap, the comparison suggests that neglecting a small core region at the centre of the star does not play a crucial role for the dynamo solution. Furthermore, these numerical findings are close to recent observational results that suggest an activity cycle of about 7 years for Proxima Centauri (Suárez Mascareño et al. 2016; Wargelin et al. 2017; Klein et al. 2020).

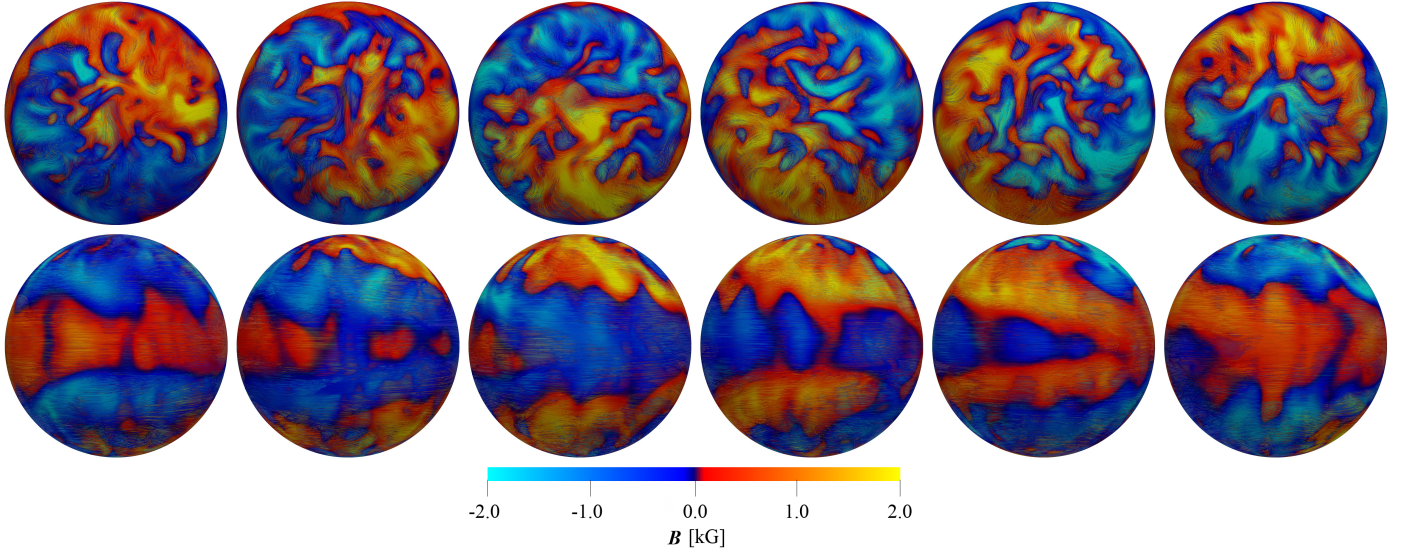


Fig. 11. Magnetic field B^{sph} at $r = R$ in run MHD5 from six snapshots separated by roughly 6 years each. The top (bottom) row shows the magnetic fields pole-on (equator-on). The colour contours and the colour-coding of the field lines indicate strength of the local radial field. The colour scale is clipped at ± 2 kG and the extrema of B_r^{sph} are ± 8.5 kG.

In another recent study, Brown et al. (2020) reported on a simulation of a fully convective star in the rapidly rotating regime. These authors quote a vorticity-based Rossby number $\text{Ro} = |\nabla \times \mathbf{u}|/2\Omega \approx 0.3$ and a velocity-based Rossby number $\text{Ro}_u = |\mathbf{u}|/2\Omega R \approx 0.01$, where $\mathbf{u} = \mathbf{U} - \bar{\mathbf{U}}$ is the fluctuating velocity, for this simulation. The inverses of the velocity- and vorticity-based Coriolis numbers of the current study, $1/\text{Co}$ and $1/\text{Co}^{(\omega)}$, are not exactly the same as the Rossby numbers of Brown et al. (2020) because they are based on the total velocity \mathbf{U} and thus overestimate the Rossby number by some factor. Thus the Ro of the simulation presented Brown et al. (2020) is most likely somewhere between the current runs MHD3 and MHD4 where $1/\text{Co}^{(\omega)} = 0.27$ and $1/\text{Co}^{(\omega)} = 0.83$.

These authors found a dynamo solution which is predominantly hemispheric. Furthermore, they explain that similar solutions are found in the parameter regime in the vicinity of the reported simulation. The current simulations do not indicate a similar behavior but sweeping conclusions cannot be made based on the very limited number of simulations done so far. There are some periods in run MHD3 where the magnetic field is predominantly hemispherical (see, Fig. 10) but such configurations cover only a small fraction of the total duration of the simulation. Furthermore, the mean magnetic field in run MHD2 is consistently stronger on the southern hemisphere (see Fig. 7). This is perhaps suggesting that oscillatory hemispheric solutions could also be realized for parameters not far away from those in the present runs MHD2 and MHD3. Another example of a possibly hemispheric dynamo was presented by Browning (2008) with velocity fluctuation-based Rossby number of $\approx 10^{-2}$, but there is not enough information regarding the time evolution of the magnetic fields to ascertain this definitively (see their Fig. 7 panels b and c).

For the rapid rotators (runs MHD4 and MHD5) the axisymmetric magnetic fields show no clear cycles while the mean fields appear to migrate predominantly toward the equator (Fig. 7). However, the fraction of the axisymmetric mean field energy in comparison to the total field energy is sharply decreasing in runs MHD[4-5] in comparison to intermediate rotation cases, see the 7th and 8th columns of Table 3. This is,

however, associated with a strong increase of the total magnetic energy (5th column of Table 3), and a closer inspection indicates that the magnetic fields in these cases have a strong non-axisymmetric contribution with a dominant $m = 1$ mode, see representative results from MHD5 in Fig. 11. This large-scale non-axisymmetric structure also drifts with respect to the rotating frame of the star. Such azimuthal dynamo waves were predicted by mean-field theory (Krause & Rädler 1980) and have more recently been reported from simulations of stellar dynamos (e.g. Käpylä et al. 2013; Cole et al. 2014; Yadav et al. 2015b; Viviani et al. 2018). In run MHD4 (MHD5) the $m = 1$ magnetic structure drifts in the retrograde direction with a period of roughly 10 (40) years. These periods are also similar to those in simulations of rapidly rotating solar-like stars (e.g. Cole et al. 2014; Viviani et al. 2018).

The rightmost panel of Fig. 8 shows that the kinetic helicity is mostly negative on the northern hemisphere in run MHD5 although the normalized values are smaller than in the less rapidly rotating cases. Due to the almost totally absent differential rotation, the most plausible dynamo mechanism in this case is an α^2 dynamo. However, more detailed information of the turbulent transport coefficients are needed to confirm this.

4. Conclusions

An updated version of the star-in-a-box model originally published by Dobler et al. (2006) was used to compute hydrodynamic and magnetohydrodynamic models of a $0.2M_{\odot}$ fully convective M5 star with various rotation rates. The current results indicate that the transition from anti-solar to solar-like differential rotation in fully convective stars occurs at a comparable rotational regime, as measured by a Coriolis number, as in simulations of partially convective stars (e.g. Gastine et al. 2014; Käpylä et al. 2014). Furthermore, the dynamo-generated large-scale magnetic fields are predominantly axisymmetric and quasi-stationary for slow rotation and axisymmetric and cyclic for intermediate rotation. For rapid rotation the large-scale fields become increasingly non-axisymmetric with a dominating low-order ($m = 1$) mode. These large-scale non-axisymmetric fields

also exhibit azimuthal dynamo waves where the large-scale magnetic structure drifts in longitude with little regard of the underlying flows (e.g. Krause & Rädler 1980; Cole et al. 2014). Remarkably, very similar transitions at comparable Coriolis numbers, have been reported from spherical shell simulations (e.g. Käpylä et al. 2013; Viviani et al. 2018). This suggests that the dynamos in fully convective stars are fundamentally the same as in partially convective stars.

The current exploratory set of simulations presented in the current study is, however, by no means exhaustive. This is illustrated by the lack of bistable dipolar and multipolar solutions (e.g. Gastine et al. 2013; Yadav et al. 2015a) and hemispheric dynamos (Brown et al. 2020) in the current set of models. A particularly interesting parameter regime is that of intermediate rotation, in the vicinity of the current run MHD3 with $P_{\text{rot}} = 43$ days, where cyclic dynamo solutions appear. Similar results have been reported from anelastic simulations in spherical shells (Yadav et al. 2016) and in full spheres (Brown et al. 2020). This similarity of solutions between widely different numerical approaches is encouraging. Furthermore, this is an interesting regime also observationally in view of the recent results on the possible activity cycles of Proxima Centauri and Ross 128 with rotation periods of the order of 100 days. Further simulations and comparisons to observations are clearly called for in this range of parameters.

Another aspect that makes fully convective stars interesting is that they are often found in post-common envelope binaries (PCEBs) (e.g. Parsons et al. 2013). The periods of many of these binaries show residue signals that indicate orbital evolution of the system. Such signals can be caused by planets although explaining their existence in such evolved systems is a problem in itself. Another explanation is that the secondary star hosts a cyclic dynamo that affects the gravitational quadrupole moment of the star which is reflected in orbit variations. This mechanism was first introduced by Applegate (1992) and more recent ideas along similar lines have decreased for example energetic requirements for orbit variations due to non-axisymmetric large-scale fields (Lanza 2020). Recent numerical simulations of Navarrete et al. (2020) demonstrated the effect of dynamo-generated magnetism on the gravitational quadrupole moment for partially convective rapidly rotating solar-like stars. Extending the study of the stellar quadrupole moment to fully convective stars is a logical step to follow in future publications.

Acknowledgements. I thank Axel Brandenburg, Fabio del Sordo, Oleg Kochukhov, Felipe Navarrete, Carolina Ortiz, Günther Rüdiger, Dominik Schleicher, and Jörn Warnecke for fruitful discussions and useful comments on the manuscript. I acknowledge the hospitality of Nordita during my visit in February-March 2020. The simulations were made using the HLRN-IV supercomputers Emmy and Lise hosted by the North German Supercomputing Alliance (HLRN) in Göttingen and Berlin, Germany. This work was supported by the Deutsche Forschungsgemeinschaft Heisenberg programme (grant No. KA 4825/2-1).

References

- Applegate, J. H. 1992, *ApJ*, 385, 621
Aurnou, J., Heimpel, M., & Wicht, J. 2007, *Icarus*, 190, 110
Baraffe, I. & Chabrier, G. 2018, *A&A*, 619, A177
Bekki, Y., Hotta, H., & Yokoyama, T. 2017, *ApJ*, 851, 74
Brandenburg, A. 2005, *ApJ*, 625, 539
Brandenburg, A. 2016, *ApJ*, 832, 6
Brandenburg, A., Johansen, A., Bourdin, P. A., et al. 2020, *arXiv:2009.08231*
Brandenburg, A., Nordlund, A., & Stein, R. F. 2000, in *Geophysical and Astrophysical Convection, Contributions from a workshop sponsored by the Geophysical Turbulence Program at the National Center for Atmospheric Research*, October, 1995. Edited by Peter A. Fox and Robert M. Kerr. Published by Gordon and Breach Science Publishers, The Netherlands, 2000, p. 85-105, ed. P. A. Fox & R. M. Kerr, 85-105
Brown, B. P., Browning, M. K., Brun, A. S., Miesch, M. S., & Toomre, J. 2010, *ApJ*, 711, 424
Brown, B. P., Miesch, M. S., Browning, M. K., Brun, A. S., & Toomre, J. 2011, *ApJ*, 731, 69
Brown, B. P., Oishi, J. S., Vasil, G. M., Lecoanet, D., & Burns, K. J. 2020, *ApJ*, 902, L3
Browning, M. K. 2008, *ApJ*, 676, 1262
Browning, M. K. 2011, in *IAU Symposium, Vol. 271, Astrophysical Dynamics: From Stars to Galaxies*, ed. N. H. Brummell, A. S. Brun, M. S. Miesch, & Y. Ponty, 69-77
Brun, A. S. & Palacios, A. 2009, *ApJ*, 702, 1078
Carroll, B. & Ostlie, D. 2013, *An Introduction to Modern Astrophysics*, Pearson custom library (Pearson)
Cattaneo, F., Brummell, N. H., Toomre, J., Malagoli, A., & Hurlburt, N. E. 1991, *ApJ*, 370, 282
Chabrier, G. & Baraffe, I. 1997, *A&A*, 327, 1039
Chabrier, G. & Baraffe, I. 2000, *ARA&A*, 38, 337
Chandrasekhar, S. 1961, *Hydrodynamic and hydromagnetic stability*
Charbonneau, P. 2020, *Living Reviews in Solar Physics*, 17, 4
Cole, E., Käpylä, P. J., Mantere, M. J., & Brandenburg, A. 2014, *ApJL*, 780, L22
Damasso, M., Del Sordo, F., Anglada-Escudé, G., et al. 2020, *Science Advances*, 6
Deardorff, J. W. 1961, *J. Atmosph. Sci.*, 18, 540
Deardorff, J. W. 1966, *J. Atmosph. Sci.*, 23, 503
Dikpati, M. & Charbonneau, P. 1999, *ApJ*, 518, 508
Dobler, W., Stix, M., & Brandenburg, A. 2006, *ApJ*, 638, 336
Donati, J.-F., Morin, J., Petit, P., et al. 2008, *MNRAS*, 390, 545
Dorch, S. B. F. 2004, *A&A*, 423, 1101
Fan, Y. & Fang, F. 2014, *ApJ*, 789, 35
Feiden, G. A., Skidmore, K., & Jao, W.-C. 2020, *arXiv:2011.07991*
Freytag, B., Steffen, M., & Dorch, B. 2002, *Astronomische Nachrichten*, 323, 213
Gastine, T., Duarte, L., & Wicht, J. 2012, *A&A*, 546, A19
Gastine, T., Morin, J., Duarte, L., et al. 2013, *A&A*, 549, L5
Gastine, T., Yadav, R. K., Morin, J., Reinert, A., & Wicht, J. 2014, *MNRAS*, 438, L76
Gilman, P. A. 1977, *Geophys. Astrophys. Fluid Dynam.*, 8, 93
Gilman, P. A. 1983, *ApJS*, 53, 243
Guerrero, G., Smolarkiewicz, P. K., de Gouveia Dal Pino, E. M., Kosovichev, A. G., & Mansour, N. N. 2016, *ApJ*, 819, 104
Guerrero, G., Smolarkiewicz, P. K., Kosovichev, A. G., & Mansour, N. N. 2013, *ApJ*, 779, 176
Hazra, G., Karak, B. B., & Choudhuri, A. R. 2014, *ApJ*, 782, 93
Hotta, H., Rempel, M., & Yokoyama, T. 2015, *ApJ*, 798, 51
Hotta, H., Rempel, M., & Yokoyama, T. 2016, *Science*, 351, 1427
Ibañez Bustos, R. V., Buccino, A. P., Flores, M., & Mauas, P. J. D. 2019, *A&A*, 628, L1
Ibañez Bustos, R. V., Buccino, A. P., Messina, S., Lanza, A. F., & Mauas, P. J. D. 2020, *arXiv:2011.10391*
Jao, W.-C., Henry, T. J., Gies, D. R., & Hambly, N. C. 2018, *ApJ*, 861, L11
Käpylä, P. J. 2019a, *A&A*, 622, A195
Käpylä, P. J. 2019b, *A&A*, 631, A122
Käpylä, P. J., Gent, F. A., Olsper, N., Käpylä, M. J., & Brandenburg, A. 2020, *Geophysical and Astrophysical Fluid Dynamics*, 114, 8
Käpylä, P. J., Käpylä, M. J., & Brandenburg, A. 2014, *A&A*, 570, A43
Käpylä, P. J., Käpylä, M. J., Olsper, N., Warnecke, J., & Brandenburg, A. 2017a, *A&A*, 599, A4
Käpylä, P. J., Korpi, M. J., Brandenburg, A., Mitra, D., & Tavakol, R. 2010, *Astron. Nachr.*, 331, 73
Käpylä, P. J., Korpi, M. J., & Tuominen, I. 2006, *Astron. Nachr.*, 327, 884
Käpylä, P. J., Mantere, M. J., & Brandenburg, A. 2011, *Astron. Nachr.*, 332, 883
Käpylä, P. J., Mantere, M. J., & Brandenburg, A. 2012, *ApJ*, 755, L22
Käpylä, P. J., Mantere, M. J., Cole, E., Warnecke, J., & Brandenburg, A. 2013, *ApJ*, 778, 41
Käpylä, P. J., Rheinhardt, M., Brandenburg, A., et al. 2017b, *ApJ*, 845, L23
Käpylä, P. J., Viviani, M., Käpylä, M. J., Brandenburg, A., & Spada, F. 2019, *Geophysical and Astrophysical Fluid Dynamics*, 113, 149
Kasting, J. F., Kopparapu, R., Ramirez, R. M., & Harman, C. E. 2014, *Proceedings of the National Academy of Science*, 111, 12641
Kichatinov, L. L. & Rüdiger, G. 1993, *A&A*, 276, 96
Klein, B., Donati, J.-F., Hébrard, É. M., et al. 2020, *arXiv:2010.14311*
Kochukhov, O. 2020, *arXiv:2011.01781*
Krause, F. & Rädler, K.-H. 1980, *Mean-field Magnetohydrodynamics and Dynamo Theory* (Oxford: Pergamon Press)
Lanza, A. F. 2020, *MNRAS*, 491, 1820
Limber, D. N. 1958, *ApJ*, 127, 363

- Morin, J., Donati, J.-F., Petit, P., et al. 2008, MNRAS, 390, 567
- Morin, J., Donati, J.-F., Petit, P., et al. 2010, MNRAS, 407, 2269
- Mullan, D. J. & Houdebine, E. R. 2020, ApJ, 891, 128
- Navarrete, F. H., Schleicher, D. R. G., Käpylä, P. J., et al. 2020, MNRAS, 491, 1043
- Nelson, N. J., Brown, B. P., Brun, A. S., Miesch, M. S., & Toomre, J. 2013, ApJ, 762, 73
- Parker, E. N. 1955, ApJ, 122, 293
- Parsons, S. G., Gänsicke, B. T., Marsh, T. R., et al. 2013, MNRAS, 429, 256
- Pipin, V. V. 2017, MNRAS, 466, 3007
- Pipin, V. V. & Kosovichev, A. G. 2011, ApJ, 727, L45
- Pipin, V. V. & Yokoi, N. 2018, ApJ, 859, 18
- Rogachevskii, I. & Kleorin, N. 2015, Journal of Plasma Physics, 81, 395810504
- Rüdiger, G. 1980, Geophys. Astrophys. Fluid Dynam., 16, 239
- Rüdiger, G. 1989, Differential Rotation and Stellar Convection. Sun and Solar-type Stars (Berlin: Akademie Verlag)
- Schrinner, M., Rädler, K.-H., Schmitt, D., Rheinhardt, M., & Christensen, U. R. 2007, Geophys. Astrophys. Fluid Dynam., 101, 81
- Simitev, R. D., Kosovichev, A. G., & Busse, F. H. 2015, ApJ, 810, 80
- Strugarek, A., Beaudoin, P., Charbonneau, P., & Brun, A. S. 2018, ApJ, 863, 35
- Suárez Mascareño, A., Rebolo, R., & González Hernández, J. I. 2016, A&A, 595, A12
- Tremblay, P.-E., Ludwig, H.-G., Freytag, B., et al. 2015, ApJ, 799, 142
- van Saders, J. L. & Pinsonneault, M. H. 2012, ApJ, 751, 98
- Viviani, M. & Käpylä, M. J. 2020, arXiv:2006.04426
- Viviani, M., Warnecke, J., Käpylä, M. J., et al. 2018, A&A, 616, A160
- Wargelin, B. J., Saar, S. H., Pojmański, G., Drake, J. J., & Kashyap, V. L. 2017, MNRAS, 464, 3281
- Warnecke, J. 2018, A&A, 616, A72
- Warnecke, J. & Käpylä, M. J. 2020, A&A, 642, A66
- Warnecke, J., Rheinhardt, M., Tuomisto, S., et al. 2018, A&A, 609, A51
- West, A. A., Weisenburger, K. L., Irwin, J., et al. 2015, ApJ, 812, 3
- Woodward, P. R., Lin, P.-H., Mao, H., Andrassy, R., & Herwig, F. 2019, in Journal of Physics Conference Series, Vol. 1225, Journal of Physics Conference Series, 012020
- Wright, N. J. & Drake, J. J. 2016, Nature, 535, 526
- Wright, N. J., Newton, E. R., Williams, P. K. G., Drake, J. J., & Yadav, R. K. 2018, MNRAS, 479, 2351
- Yadav, R. K., Christensen, U. R., Morin, J., et al. 2015a, ApJ, 813, L31
- Yadav, R. K., Christensen, U. R., Wolk, S. J., & Poppenhaeger, K. 2016, ApJ, 833, L28
- Yadav, R. K., Gastine, T., Christensen, U. R., & Reiners, A. 2015b, A&A, 573, A68
- Yoshimura, H. 1975, ApJ, 201, 740